

# Role of Structural Defects in $\text{MnO}_x$ Promoted by Ag Doping in the Catalytic Combustion of Volatile Organic Compounds and Ambient Decomposition of $\text{O}_3$

Hua Deng,<sup>†</sup> Shunyu Kang,<sup>†,‡</sup> Jinzhu Ma,<sup>\*,†,‡,§</sup> Lian Wang,<sup>§</sup> Changbin Zhang,<sup>‡,§</sup> and Hong He<sup>†,‡,§</sup>

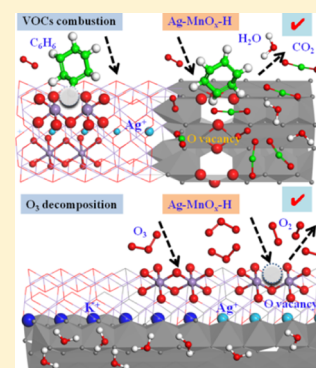
<sup>†</sup>Center for Excellence in Regional Atmospheric Environment, Key Laboratory of Urban Pollutant Conversion, Institute of Urban Environment, Chinese Academy of Sciences, Xiamen 361021, China

<sup>‡</sup>University of Chinese Academy of Sciences, Beijing 100049, China

<sup>§</sup>State Key Joint Laboratory of Environment Simulation and Pollution Control, Research Center for Eco-Environmental Sciences, Chinese Academy of Sciences, Beijing 100085, China

## Supporting Information

**ABSTRACT:** Manganese oxides are prominent candidates for the catalytic oxidation of volatile organic compounds (VOCs) or ambient decomposition of  $\text{O}_3$  individually. Here, we compared various preparation methods to create a defect-enriched Ag– $\text{MnO}_x$  nanocomposite that exhibits a remarkably multifunctional activity in VOC combustion and ozone decomposition.  $\text{Ag}^+$  ions were well-dispersed in the microtunnels of Ag– $\text{MnO}_x$ -H via hydrothermal replacement of the original  $\text{K}^+$  ions; this catalyst's benzene combustion efficiency ( $T_{90\%} = 216^\circ\text{C}$  at a space velocity of  $90\,000\text{ mL h}^{-1}\text{ g}^{-1}$ ) was comparable to that of typical noble metal catalysts. Moreover, the decomposition of ozone over the Ag– $\text{MnO}_x$ -H catalyst (space velocity =  $840\,000\text{ mL h}^{-1}\text{ g}^{-1}$ ) under a relative humidity of 60% was above 90%, indicating that it is a promising material for ozone elimination in practical application. The local structure results indicated that silver incorporation via the hydrothermal method facilitates the formation of nonstoichiometric defects in the  $\text{MnO}_x$  matrix. The large number of active oxygen species related to O vacancies appeared to play critical roles in VOC combustion; moreover, the oxygen vacancies originating from O defects were also critical in  $\text{O}_3$  abatement. This work provides multifunctional catalysts for VOC combustion and ambient  $\text{O}_3$  decomposition and may assist with the rational design of  $\text{MnO}_x$  catalysts for application in various conditions.



## 1. INTRODUCTION

Volatile organic compounds (VOCs) are among the major contributors to air pollution.<sup>12</sup> First and foremost, many VOCs are toxic and some are considered to be carcinogenic, mutagenic, or teratogenic, such as benzene,<sup>3</sup> toluene,<sup>4</sup> chlorobenzene,<sup>5</sup> and so forth. Second, VOC emissions can contribute to heavy haze and the formation of tropospheric ozone ( $\text{O}_3$ ).<sup>6,7</sup> High-concentration tropospheric ozone, formed via the photochemical reactions of primary anthropogenic pollutants involving VOCs, is a hazardous air pollutant attracting more and more attention.<sup>7,8</sup> In U.S. Environmental Protection Agency (U.S. EPA) regulations, the 8 h ozone standard level was reduced from 80 to 75 ppb in 2008, and the standard was further updated from 75 to 70 ppb in 2015. With the imposition of increasingly strict environmental protection regulations, there is more and more demand for post-treatment technologies to remove primary VOCs and secondary ozone pollution.

Various methods have been widely studied for VOCs or  $\text{O}_3$  removal individually, such as adsorption,<sup>9,10</sup> biodegradation,<sup>11</sup> catalytic oxidation,<sup>1,2</sup> or decomposition.<sup>12</sup> Among them, catalytic removal has been recognized as one of the most promising methods to remove VOCs or  $\text{O}_3$  owing to its high

efficiency and low operation and energy costs. Manganese oxides are prominent candidates for the catalytic oxidation of VOCs or decomposition of  $\text{O}_3$  because of their low cost and excellent tunable structural and physicochemical properties, as well as environmental compatibility.<sup>12–15</sup> For instance, Santos et al.<sup>16</sup> found that toluene, ethanol, and ethyl acetate could all be oxidized into  $\text{CO}_2$  at a relatively low temperature over  $\text{MnO}_2$  (OMS-2). Chen et al.<sup>17</sup> synthesized well-defined mesoporous  $\text{Mn}_2\text{O}_3$  via a novel oxalate route, which exhibited good activity for the complete oxidation of BTX (benzene, toluene, and xylene). Sphere-shaped  $\text{Mn}_3\text{O}_4$  can be prepared through the solvothermal reaction method developed by He et al.<sup>18</sup> The high content of oxygen vacancies on the surface is beneficial for the excellent low-temperature activity in the removal of methyl ethyl ketone.

On the other hand, manganese oxides are also useful and efficient for ozone decomposition. Oyama et al.<sup>12,19</sup> have pointed out that  $\text{MnO}_2$  possesses the highest activity for the

Received: March 26, 2019

Revised: July 5, 2019

Accepted: August 15, 2019

Published: August 15, 2019

catalytic removal of ozone among the common metal oxides. Zhang et al.<sup>20</sup> reported that the activity of three different MnO<sub>2</sub> crystal phases for ozone decomposition followed the order of  $\alpha > \gamma > \beta$ -MnO<sub>2</sub>, with the high activity of  $\alpha$ -MnO<sub>2</sub> attributed to having the highest number of oxygen vacancy sites. Zhu et al.<sup>21</sup> successfully tuned the concentration of oxygen vacancies of  $\alpha$ -MnO<sub>2</sub> by a vacuum deoxidation method to promote the ozone removal rate. He and co-workers<sup>22</sup> doped cerium into OMS-2 ( $\alpha$ -MnO<sub>2</sub>), which remarkably enhanced the water resistance and promoted the performance for practical ozone removal.

In brief, manganese oxides are widely used in the catalytic removal of VOCs and O<sub>3</sub>, respectively. Doping with other metals is necessary to enhance the performance in practical use. It is well known that silver can activate gaseous O<sub>2</sub>, which has been proved to be favorable for the catalytic combustion of VOCs.<sup>3,23</sup> Silver species also have been found to be among the most active components in O<sub>3</sub> decomposition.<sup>24</sup> However, the synergistic effect between silver and MnO<sub>x</sub> in VOCs and O<sub>3</sub> removal has never been scrutinized. Usually, the catalytic removal of VOCs and the decomposition of O<sub>3</sub> need completely different active sites in certain catalysts.

In this study, we report a facile method to produce a novel Ag–MnO<sub>x</sub> nanocomposite that exhibits a remarkably multifunctional activity in VOC combustion and ambient ozone decomposition. The relationships between structure and activity for Ag–MnO<sub>x</sub> were addressed via a variety of characterization techniques including X-ray diffraction (XRD), Raman spectroscopy, Brunauer–Emmett–Teller (BET) method, transmission electron microscopy (TEM), inductively coupled plasma optical emission spectrometry (ICP–OES), X-ray absorption fine structure (XAFS) analysis, X-ray photoelectron spectroscopy (XPS), H<sub>2</sub>-temperature-programmed reduction (H<sub>2</sub>-TPR), CO-temperature-programmed desorption (CO-TPD), and so forth. The correlation between the structural defects and catalytic activity for VOC oxidation and O<sub>3</sub> decomposition was unraveled. This work can benefit the design of novel MnO<sub>x</sub> catalysts for the abatement of various gaseous pollutants.

## 2. EXPERIMENTAL SECTION

**2.1. Material Preparation.** MnO<sub>x</sub> materials were prepared by the reaction between manganese acetate and potassium permanganate via a redox method, as in our previous reports.<sup>22,23</sup> Then, the samples were calcined in a furnace at 500 °C for 3 h. The final samples were denoted as MnO<sub>x</sub>. Clearly, different methods may lead to various fates of Ag species and manganese oxides. Thus, the final products may have strikingly different catalytic efficiencies in VOC oxidation and O<sub>3</sub> decomposition. To learn the interaction between silver species and MnO<sub>x</sub>, Ag–MnO<sub>x</sub> catalysts were prepared by three different methods: the hydrothermal method (denoted as Ag–MnO<sub>x</sub>-H), the impregnation method (denoted as Ag–MnO<sub>x</sub>-I), and the coprecipitation method (denoted as Ag–MnO<sub>x</sub>-C).

The detailed material preparation steps are described in the [Supporting Information](#) (Text S1).

The detailed Catalytic Evaluation section is described in the [Supporting Information](#) (Text S2).

**2.2. Material Characterization.** The X-ray absorption near-edge structure (XANES) and extended XAFS (EXAFS) of Mn-K edges were measured in transmission mode at room temperature on the BL14W1 beamline, Shanghai Synchrotron Radiation Facility, Shanghai, China.

The vapor-phase adsorption of water was studied using a 3H-2000PW Gravimetry Vapor Sorption Analyzer. To evaluate the adsorption affinity between water vapor and catalysts, Henry's constant was investigated according to the classic adsorption method. According to the properties of the virial model,<sup>25</sup> Henry's constant can be determined as follows

$$\frac{P}{q} = \frac{1}{K_H} \exp\left(2A_1q + \frac{3}{2}A_2q^2 + \frac{4}{3}A_3q^3 + \dots\right) \quad (1)$$

where  $A_1$ ,  $A_2$ , and  $A_3$  are the virial coefficients. A plot of  $\ln(P/q)$  versus the loading amount  $q$  should approach the axis linearly as  $q$  becomes close to 0, with the slope  $2A_1$  and intercept  $-\ln(K_H)$ .  $P$  is the partial pressure. A higher Henry's law constant indicates a stronger affinity between the adsorbate and the adsorbent.

The other material characterization methods are described in the [Supporting Information](#) (Text S3).

## 3. RESULTS AND DISCUSSION

**3.1. Physical Structure and Textural Properties of Catalysts.** The XRD patterns of four catalysts are shown in [Figure S1A](#). MnO<sub>x</sub>, Ag–MnO<sub>x</sub>-H, and Ag–MnO<sub>x</sub>-I exhibited similar diffraction patterns corresponding to the synthetic cryptomelane-type MnO<sub>2</sub> ( $\alpha$ -MnO<sub>2</sub>, ICDD no. 00-29-1020).<sup>22,23,26</sup> By contrast, silver coprecipitating with an Mn precursor gave rise to the product Ag–MnO<sub>x</sub>-C, which exhibited a quite different diffraction pattern. The reflections and  $2\theta$  values obtained are characteristic of bixbyite ( $\alpha$ -Mn<sub>2</sub>O<sub>3</sub>, ICDD no. 00-041-1442).<sup>27,28</sup> The lattice structure of catalysts was investigated by means of Raman spectra, as shown in [Figure S1B](#). MnO<sub>x</sub>, Ag–MnO<sub>x</sub>-H, and Ag–MnO<sub>x</sub>-I exhibit four distinct Raman peaks characteristic of pristine  $\alpha$ -MnO<sub>2</sub>/K-OMS-2 at the bands of 180, 386, 574, and 630 cm<sup>-1</sup>.<sup>23</sup> The main bands of Ag–MnO<sub>x</sub>-C at 652, 540, 480, and 308 cm<sup>-1</sup> correspond to  $\alpha$ -Mn<sub>2</sub>O<sub>3</sub>.<sup>27,28</sup> The XRD and Raman results are consistent with each other, revealing that all samples exhibit good crystallinity.

The nanostructure of the products was examined with field emission scanning electron microscopy, scanning TEM (STEM), and high-resolution TEM (HRTEM). MnO<sub>x</sub>, Ag–MnO<sub>x</sub>-H, and Ag–MnO<sub>x</sub>-I displayed a needle-like fibrous morphology, typical of K-OMS-2/ $\alpha$ -MnO<sub>2</sub> materials,<sup>29</sup> whereas Ag–MnO<sub>x</sub>-C exhibited an irregular particle morphology, as shown in [Figure S2](#). High-angle annular dark-field/STEM and energy-dispersive X-ray spectroscopy experiments were conducted to investigate the elemental distribution of Ag–O–Mn entities derived from the different preparation methods. The overlap of elemental mapping as illustrated in [Figure S3](#) reveals that Ag, O, and Mn are homogeneously dispersed in the Ag–MnO<sub>x</sub> samples.

The HRTEM images shown in [Figure 1](#) depict that the Ag-related MnO<sub>x</sub> samples exhibit well-defined lattice fringes. The width of the neighboring lattice fringes for Ag–MnO<sub>x</sub>-H and Ag–MnO<sub>x</sub>-I is about 0.72 nm, corresponding to the diffraction pattern of the (110) zone axis of tetragonal  $\alpha$ -MnO<sub>2</sub>, as shown in [Figure 1D](#).<sup>30</sup> The lattice structure agreed well with the above XRD and Raman results, confirming that the nanorod crystalline structure of  $\alpha$ -MnO<sub>2</sub> is well ordered after silver impregnation and even hydrothermal incorporation. However, it is worthy of note that the hydrothermal incorporation of silver caused the nanorod length of Ag–MnO<sub>x</sub>-H to decrease significantly (42 nm) to a value much smaller than that of

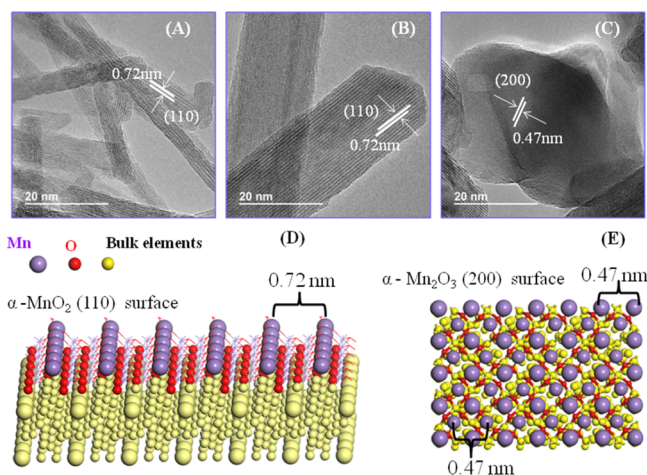


**Figure 1.** HRTEM images of different Ag–MnO<sub>x</sub> catalysts: (A) Ag–MnO<sub>x</sub>-H, (B) Ag–MnO<sub>x</sub>-I, (C) Ag–MnO<sub>x</sub>-C, (D) ideal surface (110) of  $\alpha$ -MnO<sub>2</sub>, and (E) ideal surface (200) of  $\alpha$ -Mn<sub>2</sub>O<sub>3</sub>.

MnO<sub>x</sub> (172 nm) and Ag–MnO<sub>x</sub>-I (151 nm), as shown in Figure S4. The width of the neighboring lattice fringes for Ag–MnO<sub>x</sub>-C is about 0.47 nm, corresponding to the diffraction pattern of the (200) zone axis of  $\alpha$ -Mn<sub>2</sub>O<sub>3</sub>, as shown in Figure 1E.<sup>31</sup> Consistent with the XRD and STEM results, no silver particles can be observed, confirming that the silver species are all well dispersed in/on MnO<sub>x</sub> in the MnO<sub>2</sub> and Mn<sub>2</sub>O<sub>3</sub> matrices, respectively.

The surface areas and pore volume values, together with the pore structures of different Ag–MnO<sub>x</sub> catalysts, are given in Table 1 and Figure 2A, respectively. The surface areas followed the order: Ag–MnO<sub>x</sub>-H (123.7 m<sup>2</sup>/g)  $\gg$  MnO<sub>x</sub> (59.5 m<sup>2</sup>/g) > Ag–MnO<sub>x</sub>-I (41.3 m<sup>2</sup>/g) > Ag–MnO<sub>x</sub>-C (23.9 m<sup>2</sup>/g). The dominance of the mesoporous structure for all samples could be because of the interparticle voids of the aggregated nanorods and particles.<sup>32</sup> The fact that the intraparticle mesoporosity of Ag–MnO<sub>x</sub>-H was enhanced the most was attributed to having the smallest nanorods.

It is widely known that water vapor has a strong competitive effect with VOCs and/or ozone molecules for the limited active sites on the catalysts, which is consequently detrimental to the removal performance.<sup>22,33,34</sup> Thus, the water vapor isotherms for the different Ag–MnO<sub>x</sub> catalysts were investigated (as shown in Figure 2B). To rule out the influence of multilayer adsorption of water and learn the intrinsic affinity between water vapor and the surface of the catalysts, Henry's constants were investigated according to the virial model,<sup>25</sup> and the results are exhibited in Figure 2C. The value of Henry's law constants can be ranked as follows: MnO<sub>x</sub> (1.71) > Ag–MnO<sub>x</sub>-I (0.75) > Ag–MnO<sub>x</sub>-H (0.64) > Ag–MnO<sub>x</sub>-C (0.29). A higher Henry's law constant indicates a stronger affinity between the adsorbate and the adsorbent. Silver addition significantly decreased the interaction between

water vapor and the surface of Ag–MnO<sub>x</sub> catalysts, and among these Ag–MnO<sub>x</sub>-C exhibited the best tolerance to water vapor.

To confirm the amount and position of silver in the MnO<sub>x</sub> structures, the bulk contents of Ag, Mn, and K for all the catalysts were determined by ICP–OES and presented in Table 1. The K amounts in MnO<sub>x</sub> and Ag–MnO<sub>x</sub>-I are close to the ideal content of  $\alpha$ -MnO<sub>2</sub> (5.4 wt %). However, the K content in Ag–MnO<sub>x</sub>-H was remarkably decreased by the hydrothermal incorporation of silver, as exhibited in Figure 2D. The results are consistent with another report,<sup>35</sup> confirming that silver introduced via the hydrothermal route underwent exchange with potassium ions in the tunnels of  $\alpha$ -MnO<sub>2</sub>. The XPS results of Ag 3d (as shown in Figure S5) reveal that silver species for all Ag-related samples are mostly in the form of Ag<sup>+</sup>. Although they have the same crystalline phase of  $\alpha$ -MnO<sub>2</sub>, the main difference between Ag–MnO<sub>x</sub>-H and Ag–MnO<sub>x</sub>-I is that Ag<sup>+</sup> is well dispersed in the channels of Ag–MnO<sub>x</sub>-H but anchored on the external surface of Ag–MnO<sub>x</sub>-I. As for Ag–MnO<sub>x</sub>-C, Ag species were embedded in the main structure of Mn<sub>2</sub>O<sub>3</sub> in a very dense state, as shown in Figures S3 and 2D.

### 3.2. Interaction between Silver Species and MnO<sub>x</sub>

The reducibility of the manganese oxide catalysts, an important factor known to be correlated with their redox activity, was investigated by means of H<sub>2</sub>-TPR. Meanwhile, the interaction between silver and MnO<sub>x</sub> can also be revealed. As shown in Figure 3A, silver loading via the hydrothermal route caused the main reduction peaks of Ag–MnO<sub>x</sub>-H to move to lower temperatures. However, silver incorporation via impregnation not only dramatically decreased the main reduction temperatures of MnO<sub>2</sub> but also gave rise to a new reduction peak around 172 °C. According to other reports,<sup>36</sup> the newly formed redox step could be ascribed to the reduction of silver oxide species. On the other hand, Ag–MnO<sub>x</sub>-C exhibited totally different reduction profiles because of the different main crystalline phase (bixbyite Mn<sub>2</sub>O<sub>3</sub>). A new redox process related to silver oxide species<sup>36</sup> also can be observed at 157 °C. Because of the reduction of silver oxide species appearing in Ag–MnO<sub>x</sub>-I and Ag–MnO<sub>x</sub>-C, but not for Ag–MnO<sub>x</sub>-H, we can conclude that the silver species are well dispersed and favorably interacted with the main substrate of Ag–MnO<sub>x</sub>-H. It is widely accepted that silver incorporation can significantly improve the reducibility of MnO<sub>x</sub> via the spillover of hydrogen from the silver atoms to the manganese oxides.<sup>37</sup>

Using the probe molecule, CO can reveal the intrinsic activity of oxygen species and rule out interference from the H<sub>2</sub> spillover effect.<sup>32,38</sup> Thus, a CO-TPD experiment was carried out. As clearly shown in Figure 3B, CO<sub>2</sub> (*m/z* = 44) is produced by the surface reaction between the adsorbed CO and the oxygen species of Ag–MnO<sub>x</sub> catalysts. Silver loading via the hydrothermal reaction and impregnation led to a new desorption peak of CO<sub>2</sub> in the high-temperature region around 450 °C, as shown in Figure 3B. This result unambiguously revealed that silver addition can activate the lattice oxygen

**Table 1.** Textural Parameters of All Catalysts Derived from N<sub>2</sub> Physisorption Results and the Contents of K, Mn, and Ag Metals Determined by ICP–OES

sample	BET (m <sup>2</sup> /g)	pore volume (mL/g)	Ag (wt %) (Mn/Ag)	K (wt %) (Mn/K)	Mn (wt %)
MnO <sub>x</sub>	59.5	0.6		5.2 (7.7)	55.9
Ag–MnO <sub>x</sub> -H	123.7	0.56	2.7 (39.7)	3.9 (10.1)	55.2
Ag–MnO <sub>x</sub> -I	41.3	0.41	2.4 (44.8)	5.6 (6.8)	54.3
Ag–MnO <sub>x</sub> -C	23.9	0.19	4.2 (28.3)		60.9

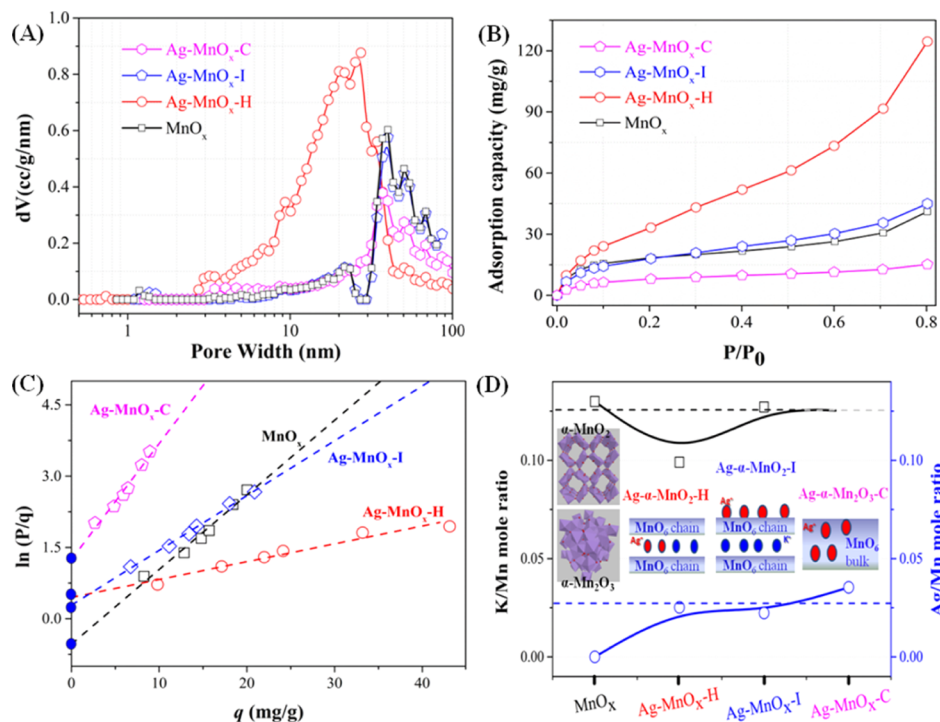


**Figure 2.** Pore distribution (A), H<sub>2</sub>O vapor adsorption isotherms at 25 °C (B), Henry's constant calculated from the virial model on the basis of water vapor isotherms (C), and elemental composition (D) for a series of Ag-MnO<sub>x</sub> catalysts.

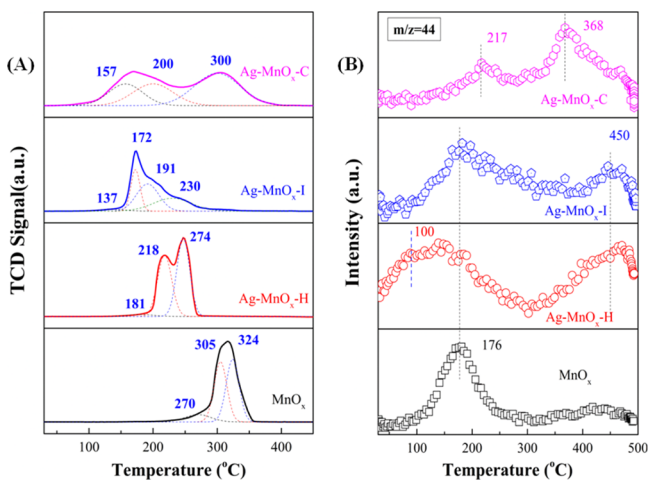


**Figure 3.** H<sub>2</sub>-TPR profiles (A) and CO<sub>2</sub> branch of CO-TPD profiles (B) of different Ag-MnO<sub>x</sub> catalysts.

species (denoted as O<sub>α</sub>). Moreover, Ag-MnO<sub>x</sub>-H has a new CO<sub>2</sub> desorption peak at even lower temperatures, around 100 °C, which could be assigned to the oxidation reaction of CO with labile surface oxygen species (denoted as O<sub>β</sub>) in the vicinity of Ag-O-Mn entities.<sup>32,38</sup> The findings suggest that surface oxygen species in the vicinity of Ag-O-Mn entities are more active than those near K-O-Mn entities. As for Ag-MnO<sub>x</sub>-C, a weak CO<sub>2</sub> desorption peak attributed to the oxidation reaction of CO with O<sub>β</sub> was observed at the higher temperature of 217 °C, whereas the main CO<sub>2</sub> desorption peaks assignable to the oxidation reaction with O<sub>α</sub> were centered at 368 °C. In brief, the XRD, Raman, HRTEM, XPS, ICP-OES, and H<sub>2</sub>-TPR results are consistent with the conclusion that silver species are intimately bonded with the MnO<sub>x</sub> matrix, as exhibited in Figure 2D. No isolated Ag<sub>2</sub>O

species could be observed in this study. Moreover, Deraz et al.<sup>39</sup> verified that the doping of Ag<sub>2</sub>O into Co<sub>3</sub>O<sub>4</sub>/MgO significantly decreased the activity of CO oxidation. Therefore, our results are in good agreement with other studies<sup>32,37,38,40</sup> reporting that highly dispersed silver species have a strong interaction with the MnO<sub>x</sub> matrix, which determines the activity of CO oxidation. Silver incorporated into the tunnel of α-MnO<sub>2</sub> not only activated lattice oxygen but also generated a number of active surface oxygen species. Thus, we can speculate that Ag-MnO<sub>x</sub>-H could be the most active candidate for benzene and/or ozone decomposition.

**3.3. Catalytic Activity of Ag-MnO<sub>x</sub> Catalysts.** The conversion of 1500 ppm C<sub>6</sub>H<sub>6</sub> over different Ag-MnO<sub>x</sub> catalysts as a function of temperature is displayed in Figure 4A. The C<sub>6</sub>H<sub>6</sub> conversion efficiency (at SV = 90 000 mL h<sup>-1</sup> g<sup>-1</sup>) can be ranked as follows: Ag-MnO<sub>x</sub>-H (T<sub>90%</sub> = 216 °C) ≫ Ag-MnO<sub>x</sub>-C (T<sub>90%</sub> = 288 °C) > MnO<sub>x</sub> (T<sub>90%</sub> = 317 °C) > Ag-MnO<sub>x</sub>-I (T<sub>90%</sub> = 341 °C). A synergistic effect derived from the reaction of silver species with α-MnO<sub>2</sub> via the hydrothermal route enhanced the catalytic performance, whereas Ag<sup>+</sup> anchored on the external surface of α-MnO<sub>2</sub> via impregnation was detrimental to benzene removal. As stated above, the Ag<sup>+</sup> ions are well dispersed in the tunnels of Ag-MnO<sub>x</sub>-H. The benzene molecule (0.55 nm) cannot gain access to the Ag<sup>+</sup> ions because of steric hindrance (opening 0.46 nm).<sup>3</sup> This is in good agreement with another report<sup>41</sup> that stated that silver implanted in the lattice of α-MnO<sub>2</sub> is more active than that anchored on the external surface. In other words, silver species should indirectly influence benzene oxidation via activating Mn polyhedra in α-MnO<sub>2</sub> rather than serving as active sites.

Ag-MnO<sub>x</sub>-H exhibited the highest C<sub>6</sub>H<sub>6</sub> conversion; so, a stability test was performed for this sample. It is clearly shown in Figure 4B that the catalyst exhibited excellent stability, maintaining above 98% C<sub>6</sub>H<sub>6</sub> conversion and CO<sub>2</sub> yield at the

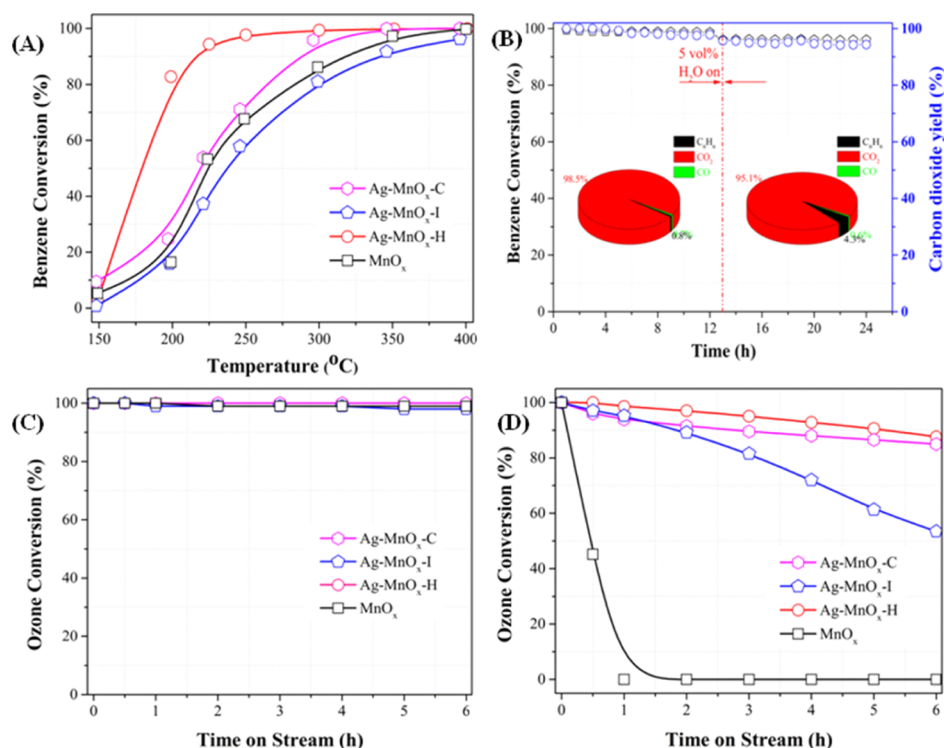


**Figure 4.** (A)  $C_6H_6$  conversion over different Ag–MnO<sub>x</sub> catalysts as a function of temperature, (B) stability test and carbon balance of the Ag–MnO<sub>x</sub>-H catalyst at 250 °C. (C) Ozone decomposition efficiency over different Ag–MnO<sub>x</sub> catalysts at 25 °C under dry conditions, (D) ozone decomposition efficiency over different Ag–MnO<sub>x</sub> catalysts under relative humidity (RH) = 60%.

temperature of 250 °C for a 12 h test. Adding 5 vol % H<sub>2</sub>O into the gas feed, the catalyst could also maintain above 95%  $C_6H_6$  conversion and CO<sub>2</sub> yield throughout another 12 h test. The sample Ag–MnO<sub>x</sub>-H was also compared with a noble metal catalyst (1 wt % Pd/Al<sub>2</sub>O<sub>3</sub>). Ag–MnO<sub>x</sub>-H clearly exhibited  $C_6H_6$  conversion very close to that of Pd/Al<sub>2</sub>O<sub>3</sub>, as shown in Figure S6, indicating that it is a promising candidate for VOC removal.

The ozone decomposition activity over different Ag–MnO<sub>x</sub> catalysts in dry or wet conditions is compared in Figure 4C,D. All catalysts exhibited a complete decomposition of 40 ppm ozone in dry conditions at a high SV value of 840 000 mL h<sup>-1</sup> g<sup>-1</sup>, as illustrated in Figure 4C. A synergistic effect derived from silver and MnO<sub>x</sub> was not prominent in dry conditions.

The coexistence of water vapor in real environments can easily lead to significant deactivation of MnO<sub>x</sub>-containing catalysts,<sup>8,22</sup> which is one of the main obstacles impeding their practical use. When the ozone inlet concentration was 40 ppm under an RH of 60% at 25 °C, ozone conversion over these catalysts decreased to a greater or lesser extent, as exhibited in Figure 4D. The optimum Ag–MnO<sub>x</sub>-H catalyst could maintain above 90% conversion even after a 6 h test, whereas the decomposition efficiency of Ag–MnO<sub>x</sub>-I decreased with time, to 60% after 6 h. However, MnO<sub>x</sub> without silver loading was by far the least active in wet conditions, completely deactivating in a 1 h test. This implies that the synergistic effect derived from silver incorporation is critical in achieving water resistance in ozone decomposition.

A summary of benzene oxidation and ozone decomposition over various catalysts is listed in Table S1. The Ag–MnO<sub>x</sub>-H catalyst exhibited an outstanding combined performance in terms of catalytic efficiency and gas hourly space velocity value among the different kinds of catalysts. The  $C_6H_6$  conversion

with O<sub>3</sub> assistance over Ag–MnO<sub>x</sub>-H was also conducted and plotted in Figure S7. It can be seen that ozone addition only slightly enhanced the activity of benzene oxidation. It is difficult to achieve complete mineralization of VOC by ozone at low temperatures because of the ambient decomposition of ozone.

**3.4. Role of Mn Polyhedra and Oxygen Species.** The efficiencies of MnO<sub>x</sub> catalysts are usually governed by their ability to cycle between different valence states (such as Mn<sup>4+</sup> and Mn<sup>3+</sup>). Even though they have the same basic unit (MnO<sub>6</sub> octahedra), the  $\alpha$ -MnO<sub>2</sub> structure (MnO<sub>x</sub>, Ag–MnO<sub>x</sub>-H, and Ag–MnO<sub>x</sub>-I) is constructed from the double chains of Mn<sup>4+</sup>O<sub>6</sub> octahedra,<sup>22,29,30</sup> whereas the  $\alpha$ -Mn<sub>2</sub>O<sub>3</sub> (Ag–MnO<sub>x</sub>-C) phase has five symmetry-inequivalent Mn<sup>3+</sup>O<sub>6</sub> sites in the unit cell.<sup>31</sup> The Mn-K XANES and the XPS of Mn 3s, illustrated in Figures S8–S10, respectively, verified the corresponding main valence state (the average oxidation state (AOS) of manganese).

The detailed degree of mixing of Mn<sup>3+</sup> and Mn<sup>4+</sup> in Ag–MnO<sub>x</sub> catalysts is exhibited in Figure 5A and Table 2. Silver impregnation did not change the degree of mixing of Mn<sup>3+</sup> and Mn<sup>4+</sup>, as MnO<sub>x</sub> and Ag–MnO<sub>x</sub>-I have similar proportions of Mn<sup>3+</sup> (12.5%) in accordance with the pristine K-OMS-2 (K<sub>1</sub>Mn<sup>3+</sup><sub>1</sub>Mn<sup>4+</sup><sub>7</sub>O<sub>16</sub>) starting material.<sup>42</sup> However, silver incorporation via the hydrothermal route caused the content of Mn<sup>3+</sup> to increase by 7.5–20%, whereas silver coprecipitation gave rise to an increment (6.4%) in Mn<sup>4+</sup> among the main Mn<sup>3+</sup>O<sub>6</sub> octahedra in Ag–MnO<sub>x</sub>-C. According to many other reports,<sup>43,44</sup> the mixing of the valence of Mn, such as the increase of Mn<sup>3+</sup> in the K-OMS-2 nanorod samples, suggests that more oxygen vacancies are generated:  $-Mn^{4+}-O^{2-}-Mn^{4+}- \rightarrow -Mn^{3+}-\square-Mn^{3+}- + 1/2O_2$ . Li et al.<sup>43</sup> proved that increasing the oxygen vacancy concentration can improve the

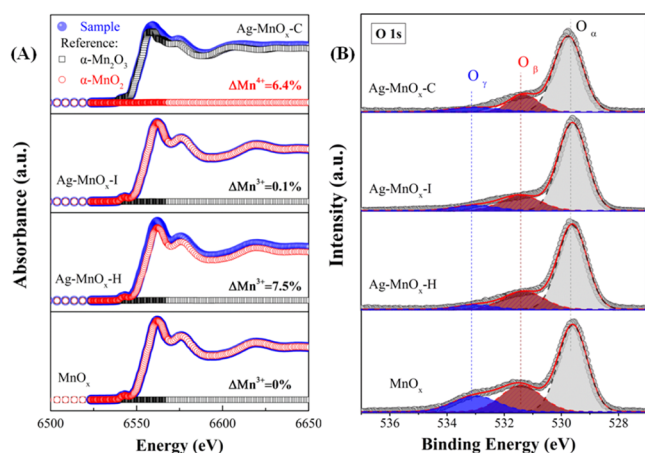


**Figure 5.** Linear combination fitting of the XANES spectra (A) and O 1s XPS spectra (B) for Ag-MnO<sub>x</sub> catalysts.

oxygen species activity. Moreover, oxygen vacancies are widely recognized as excellent sites for O<sub>3</sub> degradation in their own right.<sup>19–22</sup> All the above factors involving oxygen species stimulated by proper silver loading are thought to be vital for improving the catalytic performance.

In this regard, the oxygen species of different Ag-MnO<sub>x</sub> samples can be directly distinguished by the O 1s XPS spectra, as shown in Figure 5B. The specific peak positions and relative contents of different oxygen species are listed in Table S2. Among different oxygen species, the surface oxygen (O<sub>β</sub>, BE = 531.4 eV) was deemed to be more reactive in the elimination of VOCs owing to its high mobility.<sup>17,23,43</sup> As for the series of Ag-MnO<sub>x</sub> catalysts, MnO<sub>x</sub> has the highest amount of O<sub>β</sub> as listed in Table S1. However, Ag-MnO<sub>x</sub>-H is verified as having the most active O<sub>β</sub> as it possesses the highest amount of oxygen vacancies, as shown in Figure 5A. A portion of oxygen vacancies is formed in the microtunnel of OMS-2,<sup>43,44</sup> which is inaccessible to oxygen molecules. However, it can enhance the activity of oxygen species in the vicinity of oxygen vacancies.<sup>43,44</sup> This is the reason why the O<sub>β</sub> content of Ag-MnO<sub>x</sub>-H is lower than that of MnO<sub>x</sub>, whereas the former exhibited the highest relative activity. On the other hand, it is worth noting that silver addition caused the percentage of adsorbed water (O<sub>γ</sub>, BE = 533.0 eV) to markedly decrease by about 10% relative to the unmodified MnO<sub>x</sub>, as listed in Table S2. This is consistent with the above observation by means of Henry's law constant analysis on the basis of water vapor adsorption isotherms shown in Figure 2C, which confirms that silver doping indeed decreases the affinity between water and the surface of the catalysts.

Water vapor can easily lead to a significant deactivation of catalysts, as water vapor can occupy the active sites by competitive adsorption. Because VOC oxidation usually occurs at an elevated temperature, competitive adsorption between

water vapor and VOCs is not as significant as that in ambient ozone decomposition (Figure 4B,D). Thus, the detrimental effect of water vapor adsorption on ozone decomposition is one of the most important keys in this study. Henry's law constant was correlated with the ozone decomposition rate, as shown in Figure S11. A higher Henry's law constant indicates stronger affinity between water vapor and Ag-MnO<sub>x</sub> catalysts. As illustrated in Figure S11, the higher water vapor affinity of the catalysts causes the O<sub>3</sub> decomposition rate to decrease linearly. Thus, water vapor is a critical poisoning factor in ambient O<sub>3</sub> removal.

**3.5. Local Structure Defects in Ag-MnO<sub>x</sub>.** In solid catalysts, defects in the crystal structures, including both cationic and anionic vacancies, can act as active reaction centers.<sup>45</sup> To determine the local structure of MnO<sub>x</sub> after silver doping for catalysts synthesized via different preparation methods, EXAFS of the Mn-K edge was measured using Mn foil, MnO, Mn<sub>2</sub>O<sub>3</sub>, and α-MnO<sub>2</sub> as reference materials. Figure 6 shows the filtered *k*<sup>2</sup>-weighted EXAFS oscillations Fourier-

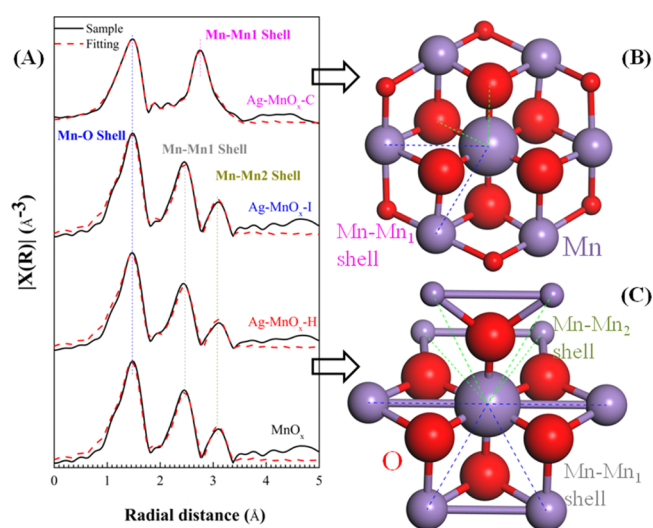


**Figure 6.** EXAFS spectra of Mn K-edge in the series of Ag-MnO<sub>x</sub> catalysts (A), ideal local structure model of α-Mn<sub>2</sub>O<sub>3</sub> (B), and ideal local structure model of α-MnO<sub>2</sub> (C).

transformed into *R* space for the series of catalysts. Good curve-fitting degrees could be obtained (Figure S12), and the curve-fitted data are also presented in Table 2.

As shown in Figure 6A, silver loading significantly decreased the coordination number (CN) of the Mn-O shell of Ag-MnO<sub>x</sub>-H (5.05) and Ag-MnO<sub>x</sub>-C (4.87) compared to the corresponding reference materials, as illustrated in Figure 6B,C and Table 2. These results unambiguously reveal that crystalline defects involving anionic vacancies (i.e., oxygen deficiency/oxygen vacancies)<sup>46</sup> are formed in the main

**Table 2.** Curve-Fitting Results of Mn-K EXAFS and Mn Ion Mixing Results for Different Ag-MnO<sub>x</sub> Samples

sample	shell	CN	<i>R</i> (Å)	σ <sup>2</sup> (×10 <sup>-3</sup> Å <sup>2</sup> )	<i>R</i> factor (%)	AOS	Mn <sup>3+</sup> (%)
α-MnO <sub>2</sub>	(Mn-O, Mn-Mn1, Mn-Mn2)	(6.00, 4.00, 4.00)	(1.92, 2.92, 3.44)			3.92	12.5
Mn <sub>2</sub> O <sub>3</sub>	(Mn-O, Mn-Mn1)	(6.00, 6.00)	(2.00, 3.10)			2.96	96.0
MnO <sub>x</sub>	(Mn-O, Mn-Mn1, Mn-Mn2)	(5.44, 3.30, 3.28)	(1.90, 2.89, 3.44)	4.32	0.78	3.93	12.5
Ag-MnO <sub>x</sub> -H	(Mn-O, Mn-Mn1, Mn-Mn2)	(5.05, 3.12, 2.66)	(1.89, 2.89, 3.45)	4.14	1.1	3.75	20.0
Ag-MnO <sub>x</sub> -I	(Mn-O, Mn-Mn1, Mn-Mn2)	(5.31, 3.52, 3.18)	(1.89, 2.89, 3.45)	4.27	0.93	3.87	12.6
Ag-MnO <sub>x</sub> -C	(Mn-O, Mn-Mn1)	(4.87, 5.54)	(1.91, 3.11)	3.90	1.2	3.07	93.6

Table 3. Specific Rates of Benzene Oxidation and Ozone Decomposition over Ag–MnO<sub>x</sub> Catalysts

sample	C <sub>6</sub> H <sub>6</sub> conversion rate at 200 °C (mmol g <sup>-1</sup> min <sup>-1</sup> )	O <sub>3</sub> decomposition rate under RH = 60% (mmol g <sup>-1</sup> min <sup>-1</sup> )	C <sub>6</sub> H <sub>6</sub> specific rate at 200 °C (μmol m <sup>-2</sup> min <sup>-1</sup> )	O <sub>3</sub> specific rate under RH = 60% (μmol m <sup>-2</sup> min <sup>-1</sup> )	C <sub>6</sub> H <sub>6</sub> TOF (min <sup>-1</sup> )	O <sub>3</sub> TOF (min <sup>-1</sup> )
MnO <sub>x</sub>	0.0164	0.0000	0.2756	0.0000	0.0162	0.0000
Ag–MnO <sub>x</sub> -H	0.0828	0.0023	0.6694	0.0182	0.0489	0.0133
Ag–MnO <sub>x</sub> -I	0.0159	0.0015	0.3850	0.0363	0.0130	0.0123
Ag–MnO <sub>x</sub> -C	0.0247	0.0021	1.0335	0.0889	0.0153	0.0132

structures of Ag–MnO<sub>x</sub>-H and Ag–MnO<sub>x</sub>-C, respectively. In addition, silver doping via the hydrothermal and coprecipitation methods also decreased the CN value in the Mn–Mn<sub>1</sub> and Mn–Mn<sub>2</sub> shells, as listed in Table 2. This finding indicates that other crystalline defects are formed involving cationic vacancies (i.e., Mn vacancies surrounded by coordinatively unsaturated oxygen<sup>47</sup>). As for Ag–MnO<sub>x</sub>-I, all coordination shells in the local structure are close to those of pristine MnO<sub>x</sub>, as presented in Table 2, which indicates that silver species anchored on the external surface via impregnation indeed do not change the local structure of α-MnO<sub>2</sub>. The role of defects promoted by silver doping will be addressed with respect to the catalytic mechanism of benzene oxidation and ozone decomposition.

**3.6. Correlation between Nonstoichiometric Defects and Activity.** To distinguish whether the enhancement of the catalytic activity of Ag–MnO<sub>x</sub> mainly arises from the increase in surface area, the specific benzene and ozone reaction rates (per unit surface area of the catalyst) are compared in Table 3. The specific rate order for benzene at 200 °C is as follows: Ag–MnO<sub>x</sub>-C > Ag–MnO<sub>x</sub>-H > Ag–MnO<sub>x</sub>-I > MnO<sub>x</sub>. In addition, the specific rate order for ozone at ambient temperature with RH = 60% can be described as Ag–MnO<sub>x</sub>-C > Ag–MnO<sub>x</sub>-I > Ag–MnO<sub>x</sub>-H > MnO<sub>x</sub>. Regardless of the silver doping method, silver addition is beneficial to the intrinsic activity of MnO<sub>x</sub>. Moreover, it is clear that Ag–MnO<sub>x</sub>-H has the highest removal rate of benzene and ozone, although the intrinsic activity per unit surface is intermediate among the materials. The high level of exposed surface area of Ag–MnO<sub>x</sub>-H appears to play a critical role in the removal of both benzene and ozone.

To reveal the intrinsic activity of Ag–MnO<sub>x</sub> catalysts precisely, the turnover frequencies (TOFs, defined as the number of reactant molecules converted per active site in a unit of time) were compared. The catalytic oxidation of VOCs over MnO<sub>x</sub> and their doped products usually proceeds via the Mars–van Krevelen mechanism.<sup>3,17,23,44</sup> Generally, the surface oxygen species (O<sub>β</sub>) have greater mobility and activity than the lattice oxygen species (O<sub>α</sub>) and may give rise to beneficial spillover phenomena at the solid surface.<sup>17,48</sup> Therefore, the availability and reactivity of O<sub>β</sub> affect the activity of manganese oxides to a great extent.<sup>49</sup> It is well known that O vacancies (V<sub>O</sub>, Mn–O shell coordination defects) are directly related to active surface oxygen species. Thus, O vacancies act as active sites for benzene oxidation. Moreover, the ozone decomposition mechanism generally involves three steps<sup>8,19,21,50</sup>



during which O vacancies (V<sub>O</sub>) act as the active sites. Thus, the ozone decomposition and benzene oxidation rate, that is,

the intrinsic activity, all depend on the properties and amounts of O vacancies. On the basis of Mn–O shell coordination defects, as shown in Table 2, the TOFs were calculated and listed in Table 3. Ag–MnO<sub>x</sub>-H exhibits the highest TOF (0.0489 min<sup>-1</sup>) for benzene oxidation, which is 3 times higher than the other Ag–MnO<sub>x</sub> catalysts. Ag–MnO<sub>x</sub>-H (0.0133 min<sup>-1</sup>) and Ag–MnO<sub>x</sub>-C (0.0132 min<sup>-1</sup>) have similar TOFs of ozone decomposition which are the highest among all samples. Considering that Ag–MnO<sub>x</sub>-H has a higher affinity with poisoning water vapor than Ag–MnO<sub>x</sub>-C (as shown in Figure 2C), we can postulate that the intrinsic activity of Ag–MnO<sub>x</sub>-H is the highest.

In conclusion, silver incorporation into MnO<sub>x</sub> via the hydrothermal method led to Ag<sup>+</sup> being well dispersed in the microtunnels of Ag–MnO<sub>x</sub>-H. The crystalline structure remained intact after silver loading, whereas nonstoichiometric changes in the local structure, that is, both Mn defects and O defects, were substantially increased. O defects play an important role in the elimination of benzene and ozone. All these results are consistent, demonstrating that Ag–MnO<sub>x</sub>-H has the highest intrinsic activity and is a promising candidate for eliminating both VOCs and ozone. This work provides multifunctional catalysts for VOC oxidation and ambient O<sub>3</sub> decomposition and may assist with the rational design of MnO<sub>x</sub> catalysts for air pollution control.

## ■ ASSOCIATED CONTENT

### 📄 Supporting Information

The Supporting Information is available free of charge on the ACS Publications website at DOI: 10.1021/acs.est.9b01822.

Characterization methods, XRD patterns, Raman spectra, FESEM images, HAADF-STEM, TEM/nanorod length distribution, XPS binding energies, and elemental mapping of different Ag–MnO<sub>x</sub> catalysts (PDF)

## ■ AUTHOR INFORMATION

### Corresponding Author

\*E-mail: jzma@rcees.ac.cn. Phone: +86-010-62849337.

### ORCID

Hua Deng: 0000-0002-5258-906X

Jinzhua Ma: 0000-0003-1878-0669

Changbin Zhang: 0000-0003-2124-0620

### Notes

The authors declare no competing financial interest.

## ■ ACKNOWLEDGMENTS

The work was supported by the National Key R&D Program of China (2017YFC0211802, 2016YFC0207104), the National Natural Science Foundation of China (51608504, 51678560, 21876191), and the Youth Innovation Promotion Association, CAS (2019306, 2017064).

## REFERENCES

- (1) Kamal, M. S.; Razzak, S. A.; Hossain, M. M. Catalytic oxidation of volatile organic compounds (VOCs) - A review. *Atmos. Environ.* **2016**, *140*, 117–134.
- (2) Zhang, Z.; Jiang, Z.; Shanguan, W. Low-temperature catalysis for VOCs removal in technology and application: A state-of-the-art review. *Catal. Today* **2016**, *264*, 270–278.
- (3) Chen, Y.; Huang, Z.; Zhou, M.; Ma, Z.; Chen, J.; Tang, X. Single Silver Adatoms on Nanostructured Manganese Oxide Surfaces: Boosting Oxygen Activation for Benzene Abatement. *Environ. Sci. Technol.* **2017**, *51*, 2304–2311.
- (4) Hu, F.; Peng, Y.; Chen, J.; Liu, S.; Song, H.; Li, J. Low content of CoOx supported on nanocrystalline CeO2 for toluene combustion: The importance of interfaces between active sites and supports. *Appl. Catal., B* **2019**, *240*, 329–336.
- (5) Chen, J.; Chen, X.; Chen, X.; Xu, W.; Xu, Z.; Jia, H.; Chen, J. Homogeneous introduction of CeOy into MnOx-based catalyst for oxidation of aromatic VOCs. *Appl. Catal., B* **2018**, *224*, 825–835.
- (6) Wu, R.; Xie, S. Spatial Distribution of Ozone Formation in China Derived from Emissions of Speciated Volatile Organic Compounds. *Environ. Sci. Technol.* **2017**, *51*, 2574–2583.
- (7) Cooper, O. R.; Parrish, D. D.; Stohl, A.; Trainer, M.; Nédélec, P.; Thouret, V.; Cammas, J. P.; Oltmans, S. J.; Johnson, B. J.; Tarasick, D.; Leblanc, T.; McDermaid, I. S.; Jaffe, D.; Gao, R.; Stith, J.; Ryerson, T.; Aikin, K.; Campos, T.; Weinheimer, A.; Avery, M. A. Increasing springtime ozone mixing ratios in the free troposphere over western North America. *Nature* **2010**, *463*, 344–348.
- (8) Li, X.; Ma, J.; Yang, L.; He, G.; Zhang, C.; Zhang, R.; He, H. Oxygen Vacancies Induced by Transition Metal Doping in  $\gamma$ -MnO<sub>2</sub> for Highly Efficient Ozone Decomposition. *Environ. Sci. Technol.* **2018**, *52*, 12685–12696.
- (9) Liu, S.; Peng, Y.; Chen, J.; Shi, W.; Yan, T.; Li, B.; Zhang, Y.; Li, J. Engineering surface functional groups on mesoporous silica: towards a humidity-resistant hydrophobic adsorbent. *J Mater Chem A* **2018**, *6*, 13769–13777.
- (10) Gall, E. T.; Corsi, R. L.; Siegel, J. A. Impact of Physical Properties on Ozone Removal by Several Porous Materials. *Environ. Sci. Technol.* **2014**, *48*, 3682–3690.
- (11) Chen, W.-H.; Yang, W.-B.; Yuan, C.-S.; Yang, J.-C.; Zhao, Q.-L. Fates of chlorinated volatile organic compounds in aerobic biological treatment processes: The effects of aeration and sludge addition. *Chemosphere* **2014**, *103*, 92–98.
- (12) Dhandapani, B.; Oyama, S. T. Gas phase ozone decomposition catalysts. *Appl. Catal., B* **1997**, *11*, 129–166.
- (13) Xu, H.; Yan, N.; Qu, Z.; Liu, W.; Mei, J.; Huang, W.; Zhao, S. Gaseous Heterogeneous Catalytic Reactions over Mn-Based Oxides for Environmental Applications: A Critical Review. *Environ. Sci. Technol.* **2017**, *51*, 8879–8892.
- (14) Huang, H.; Xu, Y.; Feng, Q.; Leung, D. Y. C. Low temperature catalytic oxidation of volatile organic compounds: a review. *Catal. Sci. Technol.* **2015**, *5*, 2649–2669.
- (15) Wang, Y.; Arandiyah, H.; Scott, J.; Bagheri, A.; Dai, H.; Amal, R. Recent advances in ordered meso/macroporous metal oxides for heterogeneous catalysis: a review. *J. Mater. Chem. A* **2017**, *5*, 8825–8846.
- (16) Santos, V. P.; Pereira, M. F. R.; Órfão, J. J. M.; Figueiredo, J. L. Mixture effects during the oxidation of toluene, ethyl acetate and ethanol over a cryptomelane catalyst. *J. Hazard. Mater.* **2011**, *185*, 1236–1240.
- (17) Tang, W.; Wu, X.; Li, D.; Wang, Z.; Liu, G.; Liu, H.; Chen, Y. Oxalate route for promoting activity of manganese oxide catalysts in total VOCs' oxidation: effect of calcination temperature and preparation method. *J. Mater. Chem. A* **2014**, *2*, 2544–2554.
- (18) Pan, H.; Jian, Y.; Chen, C.; He, C.; Hao, Z.; Shen, Z.; Liu, H. Sphere-Shaped Mn<sub>3</sub>O<sub>4</sub> Catalyst with Remarkable Low-Temperature Activity for Methyl-Ethyl-Ketone Combustion. *Environ. Sci. Technol.* **2017**, *51*, 6288–6297.
- (19) Li, W.; Gibbs, G. V.; Oyama, S. T. Mechanism of ozone decomposition on a manganese oxide catalyst. I. In situ Raman spectroscopy and ab initio molecular orbital calculations. *J. Am. Chem. Soc.* **1998**, *120*, 9041–9046.
- (20) Jia, J.; Zhang, P.; Chen, L. Catalytic decomposition of gaseous ozone over manganese dioxides with different crystal structures. *Appl. Catal., B* **2016**, *189*, 210–218.
- (21) Zhu, G.; Zhu, J.; Jiang, W.; Zhang, Z.; Wang, J.; Zhu, Y.; Zhang, Q. Surface oxygen vacancy induced alpha-MnO<sub>2</sub> nanofiber for highly efficient ozone elimination. *Appl. Catal., B* **2017**, *209*, 729–737.
- (22) Ma, J.; Wang, C.; He, H. Transition metal doped cryptomelane-type manganese oxide catalysts for ozone decomposition. *Appl. Catal., B* **2017**, *201*, 503–510.
- (23) Deng, H.; Kang, S.; Ma, J.; Zhang, C.; He, H. Silver incorporated into cryptomelane-type Manganese oxide boosts the catalytic oxidation of benzene. *Appl. Catal., B* **2018**, *239*, 214–222.
- (24) Imamura, S.; Ikebata, M.; Ito, T.; Ogita, T. Decomposition of Ozone on a Silver Catalyst. *Ind. Eng. Chem. Res.* **1991**, *30*, 217–221.
- (25) Deng, H.; Yi, H.; Tang, X.; Yu, Q.; Ning, P.; Yang, L. Adsorption equilibrium for sulfur dioxide, nitric oxide, carbon dioxide, nitrogen on 13X and 5A zeolites. *Chem. Eng. J.* **2012**, *188*, 77–85.
- (26) King'odu, C. K.; Opembe, N.; Chen, C.-H.; Ngala, K.; Huang, H.; Iyer, A.; Garces, H. F.; Suib, S. L. Manganese Oxide Octahedral Molecular Sieves (OMS-2) Multiple Framework Substitutions: A New Route to OMS-2 Particle Size and Morphology Control. *Adv. Funct. Mater.* **2011**, *21*, 312–323.
- (27) Li, Z.-Y.; Shaheer Akhtar, M.; Bui, P. T. M.; Yang, O.-B. Predominance of two dimensional (2D) Mn<sub>2</sub>O<sub>3</sub> nanowalls thin film for high performance electrochemical supercapacitors. *Chem. Eng. J.* **2017**, *330*, 1240–1247.
- (28) Xu, J.; Deng, Y.-Q.; Luo, Y.; Mao, W.; Yang, X.-J.; Han, Y.-F. Operando Raman spectroscopy and kinetic study of low-temperature CO oxidation on an alpha-Mn<sub>2</sub>O<sub>3</sub> nanocatalyst. *J. Catal.* **2013**, *300*, 225–234.
- (29) Sun, M.; Li, W.; Zhang, B.; Cheng, G.; Lan, B.; Ye, F.; Zheng, Y.; Cheng, X.; Yu, L. Enhanced catalytic performance by oxygen vacancy and active interface originated from facile reduction of OMS-2. *Chem. Eng. J.* **2018**, *331*, 626–635.
- (30) El-Sawy, A. M.; King'odu, C. K.; Kuo, C.-H.; Kriz, D. A.; Guild, C. J.; Meng, Y.; Frueh, S. J.; Dharmarathna, S.; Ehrlich, S. N.; Suib, S. L. X-ray Absorption Spectroscopic Study of a Highly Thermally Stable Manganese Oxide Octahedral Molecular Sieve (OMS-2) with High Oxygen Reduction Reaction Activity. *Chem. Mater.* **2014**, *26*, 5752–5760.
- (31) Wang, X.; Liu, Y.; Zhang, Y.; Zhang, T.; Chang, H.; Zhang, Y.; Jiang, L. Structural requirements of manganese oxides for methane oxidation: XAS spectroscopy and transition-state studies. *Appl. Catal., B* **2018**, *229*, 52–62.
- (32) Chen, J.; Tang, X.; Liu, J.; Zhan, E.; Li, J.; Huang, X.; Shen, W. Synthesis and characterization of Ag-hollandite nanofibers and its catalytic application in ethanol oxidation. *Chem. Mater.* **2007**, *19*, 4292–4299.
- (33) Deng, H.; Kang, S.; Wang, C.; He, H.; Zhang, C. Palladium supported on low-surface-area fiber-based materials for catalytic oxidation of volatile organic compounds. *Chem. Eng. J.* **2018**, *348*, 361–369.
- (34) Zhang, R.; Li, P.; Xiao, R.; Liu, N.; Chen, B. Insight into the mechanism of catalytic combustion of acrylonitrile over Cu-doped perovskites by an experimental and theoretical study. *Appl. Catal., B* **2016**, *196*, 142–154.
- (35) Yadav, G. D.; Sharma, R. V. Biomass derived chemicals: Environmentally benign process for oxidation of 5-hydroxymethyl-furfural to 2,5-diformylfuran by using nano-fibrous Ag-OMS-2-catalyst. *Appl. Catal., B* **2014**, *147*, 293–301.
- (36) Ye, Q.; Zhao, J.; Huo, F.; Wang, J.; Cheng, S.; Kang, T.; Dai, H. Nanosized Ag/alpha-MnO<sub>2</sub> catalysts highly active for the low-temperature oxidation of carbon monoxide and benzene. *Catal. Today* **2011**, *175*, 603–609.
- (37) Xu, R.; Wang, X.; Wang, D.; Zhou, K.; Li, Y. Surface structure effects in nanocrystal MnO<sub>2</sub> and Ag/MnO<sub>2</sub> catalytic oxidation of CO. *J. Catal.* **2006**, *237*, 426–430.

(38) Chen, J.; Li, J.; Li, H.; Huang, X.; Shen, W. Facile synthesis of Ag-OMS-2 nanorods and their catalytic applications in CO oxidation. *Microporous Mesoporous Mater.* **2008**, *116*, 586–592.

(39) Deraz, N.-A. M. Effect of Ag<sub>2</sub>O doping on surface and catalytic properties of cobalt-magnesia catalyts. *Mater. Lett.* **2001**, *51*, 470–477.

(40) Özacar, M.; Poyraz, A. S.; Genuino, H. C.; Kuo, C.-H.; Meng, Y.; Suib, S. L. Influence of silver on the catalytic properties of the cryptomelane and Ag-hollandite types manganese oxides OMS-2 in the low-temperature CO oxidation. *Appl. Catal., A* **2013**, *462–463*, 64–74.

(41) Hernández, W. Y.; Lopez-Gonzalez, D.; Ntais, S.; Zhao, C.; Boréave, A.; Vernoux, P. Silver-modified manganite and ferrite perovskites for catalyzed gasoline particulate filters. *Appl. Catal., B* **2018**, *226*, 202–212.

(42) Calvert, C.; Joesten, R.; Ngala, K.; Villegas, J.; Morey, A.; Shen, X.; Suib, S. L. Synthesis, Characterization, and Rietveld Refinement of Tungsten-Framework-Doped Porous Manganese Oxide (K-OMS-2) Material. *Chem. Mater.* **2008**, *20*, 6382–6388.

(43) Hou, J.; Liu, L.; Li, Y.; Mao, M.; Lv, H.; Zhao, X. Tuning the K + Concentration in the Tunnel of OMS-2 Nanorods Leads to a Significant Enhancement of the Catalytic Activity for Benzene Oxidation. *Environ. Sci. Technol.* **2013**, *47*, 13730–13736.

(44) Hou, J.; Li, Y.; Liu, L.; Ren, L.; Zhao, X. Effect of giant oxygen vacancy defects on the catalytic oxidation of OMS-2 nanorods. *J. Mater. Chem. A* **2013**, *1*, 6736–6741.

(45) Su, Y.; Lang, J.; Li, L.; Guan, K.; Du, C.; Peng, L.; Han, D.; Wang, X. Unexpected Catalytic Performance in Silent Tantalum Oxide through Nitridation and Defect Chemistry. *J. Am. Chem. Soc.* **2013**, *135*, 11433–11436.

(46) Wang, J.; Lin, L.; He, Y.; Qin, H.; Yan, S.; Yang, K.; Li, A.; Liu, J. Vacancy-assisted oxygen reduction reaction on cobalt-based catalysts in direct borohydride fuel cell revealed by in-situ XAFS and XRD. *Electrochim. Acta* **2017**, *254*, 72–78.

(47) Villalobos, M.; Bargar, J.; Sposito, G. Mechanisms of Pb(II) sorption on a biogenic manganese oxide. *Environ. Sci. Technol.* **2005**, *39*, 569–576.

(48) Piumetti, M.; Fino, D.; Russo, N. Mesoporous manganese oxides prepared by solution combustion synthesis as catalysts for the total oxidation of VOCs. *Appl. Catal., B* **2015**, *163*, 277–287.

(49) Yang, Y.; Huang, J.; Zhang, S.; Wang, S.; Deng, S.; Wang, B.; Yu, G. Catalytic removal of gaseous HCBz on Cu doped OMS: Effect of Cu location on catalytic performance. *Appl. Catal., B* **2014**, *150–151*, 167–178.

(50) Li, W.; Oyama, S. T. Mechanism of ozone decomposition on a manganese oxide catalyst. 2. Steady-state and transient kinetic studies. *J. Am. Chem. Soc.* **1998**, *120*, 9047–9052.